Phase-Field Modeling for Intercritical Annealing of a Dual-Phase Steel

2 authors, including:

Phase-Field Modeling for Intercritical Annealing of a Dual-Phase Steel

BENQIANG ZHU and MATTHIAS MILITZER

A phase-field model has been developed to describe microstructure evolution during intercritical annealing of a commercial DP600 dual-phase steel. The simulations emphasize the interaction between ferrite recrystallization and austenite formation from a cold-rolled pearlite/ferrite microstructure at high heating rates. The austenite-ferrite transformations are assumed to occur under conditions where only carbon partitions between the phases by long-range diffusion. A solute drag model has been integrated with the phase-field model to describe the effect of substitutional alloying elements on the migration of the ferrite/austenite interface. Experimental results including recrystallization and transformation kinetics as well as austenite morphology have been successfully described by carefully adjusting both the austenite nucleation scenario and the interface mobilities.

I. INTRODUCTION

DUAL-PHASE steels are advanced high-strength steels that are now widely used in the automotive industry. Compared with conventional high-strength steels, *e.g.*, high-strength low-alloy (HSLA) steels, dual-phase steels have a better combination of strength and formability as well as higher crashworthiness. There are two principal processing routes to produce DP steel sheets: (i) controlled cooling from the austenite phase (hot-rolled products); (ii) intercritical annealing of cold-rolled steels in continuous annealing or hot-dip galvanizing lines. In particular, the intercritical annealing route is of primary interest to produce sheets with the required surface quality and thickness of 1 mm and below.

A number of microstructure process models were developed for controlled run-out table cooling of hot-rolled DP steels.[1–3] There is, however, a remarkable lack of such models for intercritical annealing. Bos *et al.* developed a 3D cellular automaton model describing the microstructure evolution during intercritical annealing of a cold-rolled Fe-0.1 wt pctC-1.5 wt pctMn steel with an initial pearlite/ferrite microstructure.[4] The model consists of sub-models for ferrite recrystallization, austenite formation, and the austenite-to-ferrite transformation. These microstructure phenomena are assumed to occur in sequence rather than concurrently, *i.e.*, the potential interaction of ferrite recrystallization and austenite formation is not taken into account. Moreover, it is assumed that the ferrite-to-austenite transformation is interface controlled even though the

transformation is typically of mixed-mode character in a low-carbon steel, *i.e.*, both interface reaction and long-range diffusion would have to be considered. Nevertheless, the model provides a framework for meso-scale simulation of microstructure evolution during intercritical annealing.

In contrast to Bos *et al.*, Rudnizki *et al.* simulated austenite formation as a transformation controlled by long-range diffusion of carbon.[5] Using the commercial phase-field package MICRESS®, they described austenite formation in a Fe-0.1 wt pctC-1.65 wt pctMn steel from an annealed pearlite/ferrite microstructure. Austenite nucleation was assumed to take place within pearlite, and nucleation at ferrite grain boundaries was not considered. The modeling of the pearlite-to-austenite transformation and the ferrite-to-austenite transformation was performed separately in two steps, *i.e.*, quick growth of austenite into pearlite which is assumed to be an effective phase with eutectoid carbon composition followed by growth into ferrite. A sufficiently high interface mobility was adopted such that the ferrite-to-austenite transformation occurs in a carbon diffusion-controlled mode. Here, two equilibrium modes, *i.e.*, para-equilibrium (PE) and non-partition local equilibrium (NPLE), were used to simulate the transformation kinetics. It was found that the model with the NPLE assumption describes the transformation kinetics that is consistent with experimental observations for one selected heating scenario. The applicability of the model to different heat treatment scenarios was not reported.

Recently, the interaction of austenite formation with concurrent ferrite recrystallization has drawn much attention as it significantly affects the final dual-phase microstructure opening new avenues to generate dual-phase steels with improved properties.[6–8] Zheng and Raabe developed a 2D cellular automaton model to simulate the interaction of ferrite recrystallization and austenite formation during intercritical annealing

BENQIANG ZHU, Ph.D. Student, and MATTHIAS MILITZER, Professor, are with The Center for Metallurgical Process Engineering, The University of British Columbia, 309-6350 Stores Road, Vancouver, BC V6T 1Z4, Canada. Contact e-mail: zhubenqiang@ gmail.com

of a cold-rolled low-carbon steel (Fe-0.08 wt pctC-1.75 wt pctMn).[9] The simulation replicated a number of experimental observations of Azizi-Alizamini et al.,[7] e.g., austenite nucleation occurs both in pearlite and at ferrite grain boundaries. Further, some recrystallization fronts may be pinned by austenite grains whereas others cannot be pinned such that selected austenite grains can appear as islands in ferrite grains even though no intragranular nucleation mode is operative. However, the model parameters were not tuned to replicate the experimentally measured transformation kinetics.

The present paper is devoted to a stand-alone phase-field model that can describe both the experimentally measured transformation kinetics and microstructural morphologies during a variety of intercritical annealing scenarios of a dual-phase steel. The proposed approach builds on previous simulations of recrystallization[10] by combining sub-models for ferrite recrystallization, austenite formation, and decomposition of intercritical austenite. The model is designed to describe the possible interaction of ferrite recrystallization and austenite formation. Furthermore, a solute drag model is integrated with the phase-field model to account for the influence of substitutional alloying elements on the migration of the ferrite/austenite interfaces. The model is applied to a low-carbon steel that is used in the steel industry to produce DP600 steel (Fe-0.11 wt pctC-1.86 wt pctMn-0.34 wt pctCr-0.16 wt pctSi). The initial microstructure consists of 15 pct pearlite and 85 pct ferrite and is 50 pct cold-rolled. The phase-field model is benchmarked and validated with the experimental data of Kulakov.[10]

II. MODEL

A. Basics of the Multi-Phase-Field Model

The multi-phase-field model developed originally by Steinbach et al.[11,12] is employed in this work to describe the microstructure evolution in terms of both recrystallization kinetics and the resulting grain morphologies. In the model, each grain i is defined by its own phase-field parameter ϕ_i. Inside grain i, ϕ_i is equal to 1 while it is 0 outside the grain. Within the interface of width η, ϕ_i changes continuously from 0 to 1. The phase-field parameter ϕ_i represents the local fraction of each grain which implies that there exists the constraint of $\sum \phi_i = 1$. Each grain can be assigned a set of attributes, e.g., phase, crystallographic orientation, and stored energy. The temporal evolution of each field variable is described by the superposition of the pair-wise interaction with its neighboring grains:

$$\frac{d\phi_i}{dt} = \sum_{i \neq j} m_{ij} \left\{ \sigma_{ij} \left[(\phi_j \nabla^2 \phi_i - \phi_i \nabla^2 \phi_j) + \frac{\pi^2}{2\eta^2} (\phi_i - \phi_j) \right] + \frac{\pi}{\eta} \sqrt{\phi_i \phi_j} \Delta G_{ij} \right\},$$ [1]

where m_{ij} is the interfacial mobility, σ_{ij} is the interfacial energy, and ΔG_{ij} is the driving pressure. The mobilities are assumed to obey an Arrhenius relationship, i.e.,

$$m_{ij} = m_{ij}^0 \exp\left(-\frac{Q_{ij}}{RT} \right),$$ [2]

where m_{ij}^0 is the pre-factor, Q_{ij} is the activation energy, T is the temperature, and R is the ideal gas constant.

Further, the phase-field model is coupled with the diffusion equation for carbon

$$\frac{\partial C}{\partial t} = \nabla \left[\sum_i D_i \phi_i \nabla C_i \right]$$ [3]

to account for long-range diffusion during phase transformation. Here D_i is the carbon diffusivity in grain i and C is the local carbon concentration which, in the interface region, is the sum of carbon concentrations C_i weighted with the phase-field parameter:

$$C = \sum_i \phi_i C_i$$ [4]

The diffusion coefficient depends on the phase (i.e., ferrite or austenite) of each grain but for simplicity is taken to be independent of carbon concentration.

A finite-difference method is used to solve the phase-field and diffusion equations numerically. A parallel computer program written with MPI and OpenMP is used to implement simulations efficiently.

B. Initial Microstructure

A simulation domain of 100 μm $\times$ 100 μm with a grid size of 0.1 μm and periodic boundary conditions are used here. The interface thickness η is set to 0.5 μm, i.e., there are five grid points through the interface. The initial deformed structure is constructed using Voronoi tessellation[13] that conforms to the experimental measurements,[10] e.g., spacing of pearlite bands (14 μm) and the average ferrite grain size (9.5 μm). Pearlite is assumed to be a single "effective" phase with eutectoid carbon content.[5,9] It is further assumed that the initial distribution of substitutional elements is uniform, and carbon concentrations are 0.63 wt pct in pearlite and 0.012 wt pct in ferrite which correspond to the para-equilibrium phase diagram at the eutectoid temperature. The constructed microstructure is shown in Figure 1.

The stored energy, mainly in the form of dislocations, is induced by cold deformation. The contribution of internal stresses to the stored energy is negligible.[14] The input of stored energy is based on our previous work.[13] It is assumed that the stored energy in each grain is uniform but varies among grains. The distribution of the stored energy is calculated with the orientation density function (ODF) measured by EBSD,[15] based on the hypothesis that the stored energy in one grain is proportional to the Taylor factor associated with the crystallographic orientation of that grain. The magnitude of the stored energy is scaled such that the average stored energy E_{avg} is consistent with the value of 2 MJ/m^3 that was estimated with hardness tests by Kulakov.[10] The
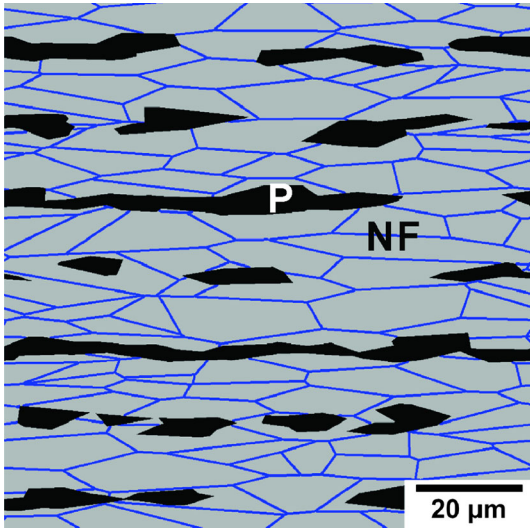
Fig. 1—Initial cold-rolled structure (P: pearlite; NF: non-recrystallized ferrite).
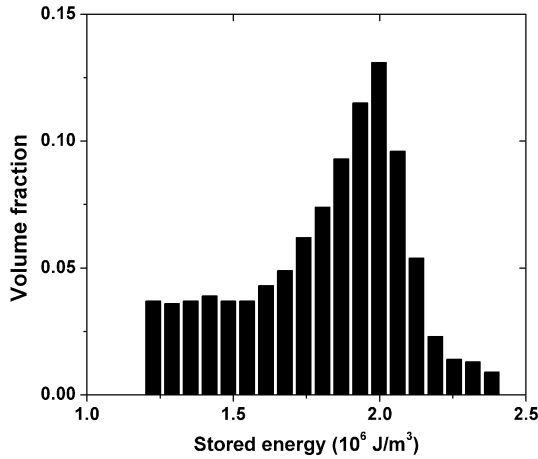

Fig. 2—Stored energy distribution in the cold-rolled material.

calculated stored energy distribution is shown in Figure 2. The present approach of stored energy estimation is a first-order approximation. Alternatively, some other experimental and modeling techniques can be used which can take variation of stored energy within a given grain into account, e.g., EBSD image quality[16] and crystal plasticity finite-element modeling.[17,18]

C. Ferrite Recrystallization

The approach to simulate ferrite recrystallization is based on our previous phase-field model for a ferrite-pearlite-bainite microstructure.[13] Only ferrite recrystallization is considered, while microstructure evolution in pearlite, e.g., cementite dissolution and spheroidization, is not taken into account. Moreover, the crystallographic orientation of recrystallizing grains is not considered in the model. Thus, low-angle and high-angle grain boundaries are not distinguished. Instead, all grain boundaries are assumed to be high-angle such that the boundary energy and mobility are not functions of misorientation.[16] This assumption is
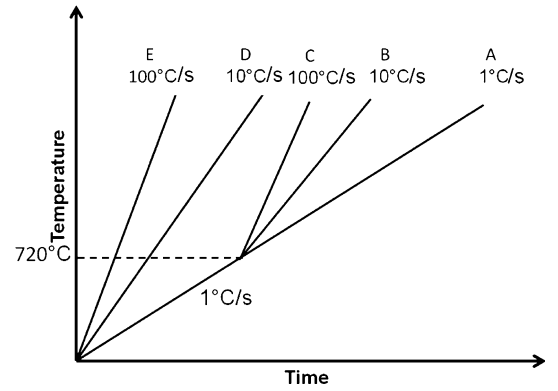

Fig. 3—Heating scenarios in the simulations.

supported by the experimental observation of similarities of the recrystallization textures at early and final recrystallization stages in low-carbon steels by Sanchez-Araiza et al.,[19] which implies that selective growth of recrystallizing grains due to interface anisotropy is not significant.

It is postulated that site-saturated nucleation of dislocation-free ferrite takes place in grains where the stored energy exceeds a critical value E*, i.e.,

$$E > E^* \quad [5]$$

The nuclei number N_{RX}^{α} in the domain is taken to be the number of grains per area as estimated from experimental measurements of the recrystallized ferrite grain size. The grain boundary energy is assumed to be 0.8 J/m^2.[13] The value of E*, the pre-factor $m_{\alpha\alpha}^0$, and the activation energy $Q_{\alpha\alpha}$ of the mobility are adjustable and determined from the experimental recrystallization kinetics at three isothermal conditions [873 K, 898 K, and 923 K (600 °C, 625 °C, and 650 °C)].

D. Austenite Formation

In this study, five heating scenarios are selected from the experimental work[10] to benchmark the phase-field model (Figure 3). The step-heating simulations (A–C) are intended to investigate the effect of heating rate on austenite formation in a well-annealed microstructure. On the other hand, the continuous heating simulations (D–E) are aimed at studying the interaction between ferrite recrystallization and austenite formation. Austenite formation is assumed to occur under para-equilibrium conditions.

Savran et al.[20] conducted dedicated studies on austenite nucleation and observed continuous nucleation in a low-carbon steel. These results are in qualitative agreement with the observations by Kulakov[10] in the steel investigated here. Similar to previous observations, Kulakov found rapid pearlite-to-austenite transformation followed by a more gradual transformation of ferrite to austenite. Further, austenite nucleation was observed to occur at both pearlite/ferrite interfaces and ferrite grain boundaries. Thus, two separate nucleation models are postulated for the present simulations.

Site saturation is assumed for austenite nucleation at pearlite/ferrite interfaces with a nucleus density that is, based on experimental observation, independent of

heating scenarios. A nuclei density of 0.024 μm^{-2}[15] is adopted, and the nucleation temperature is set to 1003 K (730 °C), in agreement with the measured austenite start temperature at the lowest investigated heating rate, i.e., 1 K/s (°C/s).[10] The specific nucleation sites at the pearlite/ferrite interfaces are randomly selected.

On the other hand, classical nucleation theory is employed to describe the more gradual austenite nucleation at ferrite grain boundaries:

$$\frac{dN}{dt} = \lambda N_P(t) \exp\left(-\frac{\frac{\psi}{\Delta g^2} + Q_d}{kT}\right), \qquad [6]$$

where λ is a constant related to atom jump frequency, $N_P(t)$ is the number of potential nucleation sites that is proportional to the total length of ferrite grain boundaries in the 2D simulation domain and decreases with time t as more and more nuclei occupy the ferrite grain boundaries, ψ is a constant related to the assumed nucleus shape and interface properties (2.1×10^{-6} J^3/m^6[21]), Δg is the driving force for nucleation which depends on carbon concentration in ferrite and temperature as calculated with Thermo-calc® using the TCFE7 database, and Q_d is the activation energy of iron diffusion in ferrite (3.9×10^{-19} J[20]). The average carbon concentration in ferrite is used to calculate the driving force for nucleation Δg, because the carbon has an approximately uniform concentration in ferrite due to its low solubility and high diffusivity in ferrite. The factor λ is kept adjustable and tuned with the experimentally measured austenite grain size for the fastest investigated heating scenario with a heating rate of 100 K/s (°C/s) where grain coarsening is assumed to be negligible. In the case of concurrent ferrite recrystallization and austenite formation, it is assumed that migrating recrystallization fronts are not potential nucleation sites.

Further, it was observed that austenite grains formed at ferrite grain boundaries grow mainly into one of the two neighboring ferrite grains.[22] This observation can be rationalized based on special crystallographic orientation relationships between the austenite grain and one of the adjacent ferrite grains, e.g., the Kurdjumov–Sachs (K–S) relationship, making this portion of the α/γ interface semi-coherent and of low mobility. In the current model, it is postulated that all the austenite nuclei on a boundary segment between two ferrite grains $\alpha 1$ and $\alpha 2$ have a special orientation relationship with one specific ferrite grain (e.g., $\alpha 1$) but not with the other one ($\alpha 2$), such that the mobility of the $\alpha 1/\gamma$ interfaces is taken as 5 pct of that of the $\alpha 2/\gamma$ interfaces, leading to dominant growth of austenite grains into $\alpha 2$. It is a random selection in the model as to whether $\alpha 1$ or $\alpha 2$ is the grain with which austenite has a special orientation relationship.

For both types of nucleation sites, the nuclei are introduced into the simulation domain as circular grains with a diameter of 0.1 μm. The dependence of nucleus morphology on interface energies, i.e., the wetting phenomenon,[23,24] is not taken into account here.

Transformation of pearlite to austenite is assumed to be interface controlled with a driving force of

$$\Delta G_{P\gamma}(T) = G_P(T) - G_\gamma(T), \qquad [7]$$

where G_P and G_γ are the Gibbs free energies of pearlite and austenite, respectively, as determined with Thermo-calc®. Since pearlite is not a phase but a mixture of ferrite and cementite, its Gibbs free energy is calculated from

$$G_P(T) = f_\alpha G_a(T) + (1 - f_\alpha)G_\theta(T), \qquad [8]$$

where f_α is the molar fraction of ferrite in eutectoid pearlite; G_α and G_θ are the molar Gibbs free energy for ferrite and cementite, respectively.

The P/γ interface energy is taken as 0.9 J/m^2.[5] The P/γ interface mobility is adjusted to fit the pearlite-to-austenite transformation kinetics for various heating scenarios (A–E).

The chemical driving pressure for ferrite/austenite transformation is described by a mixed-mode model:

$$\Delta G_{\alpha\gamma}^t = \chi_{\alpha\gamma}\left(c_{\gamma/\alpha} - c_{\gamma/\alpha}^*\right), \qquad [9]$$

where $\chi_{\alpha\gamma}$ is a proportionality factor that is calculated with Thermo-calc®, $c_{\gamma/\alpha}$ is the interfacial carbon concentration in austenite, and $c_{\gamma/\alpha}^*$ is the para-equilibrium carbon concentration in austenite. The stored energy in deformed ferrite grains is also included in the total driving pressure.

In this study, the solute drag pressure of the main substitutional alloying element, i.e., Mn, is taken into account. Therefore, the effective driving force on the ferrite/austenite interface in the phase-field equation (Eq. [1]) is given by

$$\Delta G_{\alpha\gamma} = \Delta G_{\alpha\gamma}^t - \Delta G_{sd}, \qquad [10]$$

where ΔG_{sd} is the solute drag force that is calculated with a separate model as described in Section II–E.

The ferrite/austenite interface energy is 0.5 J/m^2.[25] The activation energy of interface mobility is taken to be 140 kJ/mol,[25] while the pre-factor is kept adjustable and tuned with experimentally measured transformation kinetics for different heating rates (A–C).

E. Solute Drag Model

Frequently, solute atoms tend to segregate to interfaces to relieve elastic stress because of the excess volume in the interface region. When the interface is moving, the segregated solute atoms tend to follow and, as a result, exert a drag force on the interface. The solute drag concept was first introduced into modeling grain boundary migration.[26,27]

In this study, the solute drag model is based on the Gibbs-energy dissipation theory developed by Hillert.[26] The diffusion potential μ_M^{dif} of solute Mn across the interface is obtained from

$$\mu_M^{dif} = \mu_M - \mu_{Fe} \approx E(y) + RT \ln x_M, \qquad [11]$$

where x_M is the molar fraction of Mn in the substitutional sublattice, μ_M and μ_{Fe} are the chemical potentials of Mn and Fe in the interface, and $E(y)$ is the interaction potential of solute Mn with the interface, which is assumed to be of a wedge-shaped profile across the interface (Figure 4). Here, the minimum in the potential profile represents the binding energy E_0, and $2\Delta E$ is the potential difference between ferrite and austenite which is calculated with Thermo-calc®.

The concentration profile $x_M(y)$ of the substitutional element Mn across an interface moving with a velocity of V is given by

$$D_M^{tr} \frac{\partial x_M}{\partial y} + \frac{D_M^{tr} x_M}{RT} \frac{\partial E}{\partial y} + V(x_M - x_M^0) = 0, \quad [12]$$

where D_M^{tr} is the diffusivity of solute Mn across the austenite/ferrite interface, and x_M^0 is the concentration in the bulk. An analytical solution of the concentration profile can be derived:[28]

$$\begin{cases} \frac{x_M}{x_M^0} = \frac{1 + a\exp(-v(1+a)(Y+1))}{1+a} & -1 < Y < 0 \\ \frac{x_M}{x_M^0} = \frac{1 + a + (a(1+b)\exp(-v(1+a)) + b - a)\exp(-v(1+b)Y)}{(1+a)(1+b)} & 0 < Y < 1 \end{cases}$$

$$[13]$$

where

$$v = \frac{V\Lambda}{D_M^{tr}}$$

$$Y = \frac{y}{\Lambda}$$

$$a = \frac{1}{v} \times \frac{(\Delta E - E_0)}{RT}$$

$$b = \frac{1}{v} \times \frac{(\Delta E + E_0)}{RT}$$

Here, 2Λ denotes the 'real' interface thickness which is different from the 'numerical' interface thickness η in the phase-field equation.

The solute drag pressure can be calculated from

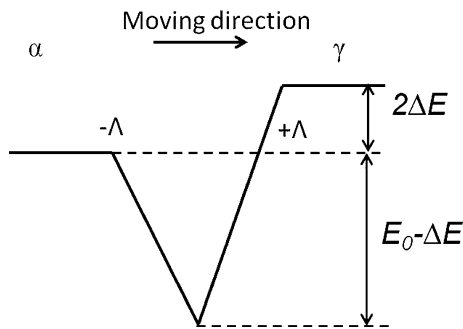$$\Delta G_{sd} = -\int_{-\Lambda}^{+\Lambda} (x_M - x_M^0) \frac{dE(y)}{dy} dy. \quad [14]$$

Fig. 4—Interaction potential of solute at the interface (Λ is half thickness of the interface, E_0 is binding energy, and $2\Delta E$ is difference of diffusion potential between austenite and ferrite in standard state).

The real interface thickness is assumed to be 1 nm.[29] The trans-interface diffusivity of Mn is taken as the geometric average of the bulk diffusivities in ferrite and austenite.[29] A value of 10 kJ/mol[30] is used for the binding energy.

F. Grain Growth

Grain growth of both ferrite and austenite is included in the phase-field model. The interface energy and mobility of the ferrite grain boundary are set in the recrystallization model (Section II–C). The grain boundary energy of austenite is taken to be 0.7 J/m^2.[31] The activation energy $Q_{\gamma\gamma}$ of the grain boundary mobility in austenite is assumed to be 185 kJ/mol,[31] and the pre-factor is adjusted such that the final austenite grain size is consistent with experimental measurements of complete austenite formation.

G. Austenite-to-Ferrite Transformation

In the cooling process of an intercritical annealing cycle, austenite will transform back to ferrite partially by reversing the moving direction of austenite/ferrite interfaces without ferrite nucleation, which is called epitaxial ferrite growth. The formulations proposed for austenite formation are used for epitaxial ferrite growth, e.g., calculation of driving and solute drag pressures as well as the austenite/ferrite interface mobility.

III. SIMULATION RESULTS AND DISCUSSION

A. Ferrite Recrystallization

The nuclei density N_{RX}^α, the critical stored energy for nucleation E^*, the pre-factor $m_{\alpha\alpha}^0$, and the activation energy $Q_{\alpha\alpha}$ of the grain boundary mobility are fitted with the experimental data for three isothermal conditions [873 K, 898 K, and 923 K (600 °C, 625 °C, and 650 °C)] as follows. The nuclei density N_{RX}^α is adjusted to replicate the average grain size after full recrystallization that is independent of temperature.[15] The nucleation parameter E^* determines primarily the shape of the recrystallization curve with time that can be represented by the Johnson–Mehl–Avrami–Kolmogorov (JMAK) exponent. Thus, the value of E^* is adjusted such that the JMAK exponent of the simulated recrystallization kinetics is consistent with the average JMAK exponent of the experimentally measured kinetics for the three temperatures. The grain boundary mobility is subsequently adjusted to fit the recrystallization kinetics on the time scale for each temperature, because it only influences the time scale of recrystallization kinetics. Using the values of mobility for the three temperatures, the pre-factor $m_{\alpha\alpha}^0$ and the activation energy $Q_{\alpha\alpha}$ of the interface mobility are finally fitted with the Arrhenius relationship (Eq. [2]).

Figure 5(a) compares simulation results with experimental data for isothermal recrystallization kinetics. These simulations were used to determine appropriate values of nucleation parameters and grain boundary
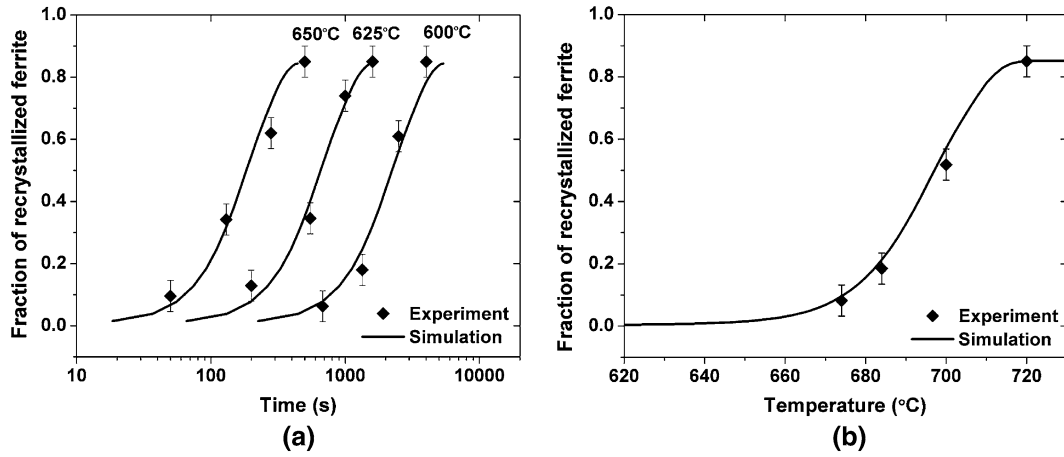
Fig. 5—Comparison of calculated recrystallization kinetics with experimental data for isothermal (a) and non-isothermal (b), heating rate: 1 °C/s) tests.

Table I.   Values of Adjustable Parameters in the Model of Ferrite Recrystallization

Parameter	Symbol	Value
Critical stored energy for recrystallization nucleation	E^* (MJ/m^3)	1.7
Recrystallized ferrite nuclei density (μm^{-2})	N_{RX}^α (μm^{-2})	1.7×10^{-2}
Pre-factor of the mobility of ferrite grain boundaries	$m_{\alpha\alpha}^0$ (m^4/Js)	1.2×10^5
Activation energy of the mobility of ferrite grain boundaries	$Q_{\alpha\alpha}$ (kJ/mol)	325

mobility (Table I) to obtain agreement between experiment and simulation in terms of kinetics and ferrite grain size which is independent of temperature 7.6 ± 0.3 μm in the simulations and 7.7 ± 0.5 μm in the experiments.[14]

Using the tuning parameters shown in Table I, the model is used to predict the recrystallization kinetics during continuous heating with a heating rate of 1 K/s (°C/s). As illustrated in Figure 5(b), excellent agreement with the experimental data is obtained. The simulated grain size at 993 K (720 °C) (7.6 μm) is also consistent with the experimental measurement (8.0 μm). Therefore, the recrystallization model is considered to be reliable and robust to describe ferrite recrystallization for other processing routes, e.g., heating at 10 to 100 K/s (°C/s).

B. Austenite Formation During Step Heating

Simulations of step-heating scenarios (A–C) are carried out first to study the effect of heating rate on austenite formation in a well-annealed microstructure where ferrite recrystallization is complete before the onset of austenite formation.

The fitting procedure of the adjustable parameters in the model, i.e., the nucleation parameter λ that affects the nuclei density at ferrite grain boundaries (Eq. [6]) and the interface mobilities ($m_{\gamma\gamma}$, $m_{P\gamma}$, and $m_{\alpha\gamma}$), is as follows. First, it is reasonable to assume that austenite grain growth is negligible in Case C with a heating rate of 100 K/s (°C/s). Thus, the average austenite grain size after full austenitization in Case C can be used to estimate the total nuclei density during austenite formation. Further, according to the metallographic

measurements at early stages of austenite formation by Kulakov,[15] the nuclei density in pearlite regions is 0.024 μm^{-2} and independent of heating rate. Based on the total nuclei density and the nuclei density in pearlite regions in Case C, the nuclei density at ferrite grain boundaries in Case C can be calculated and used to fit the nucleation parameter λ. Once the nucleation parameter λ is determined, the average austenite grain sizes in Case A and B (heating at 1 and 10 K/s (°C/s), respectively) will depend only on the mobility of austenite grain boundaries $m_{\gamma\gamma}$ that affects the rate of austenite grain growth. Thus, with the activation energy $Q_{\gamma\gamma}$ set to 185 kJ/mol,[31] the pre-factor $m_{\gamma\gamma}^0$ is adjusted such that the average austenite grain sizes in simulations are consistent with the experimental measurements in Case A and B. Because the pearlite/austenite interface mobility affects the pearlite-to-austenite transformation rate, both the pre-factor $m_{P\gamma}^0$ and the activation energy $Q_{P\gamma}$ of the pearlite/austenite interface mobility are fitted with the measured transformation kinetics at the early stage of austenite formation (austenite fraction below 0.20) where the pearlite-to-austenite transformation is dominant. Similarly, with the activation energy of the ferrite/austenite interface mobility $Q_{\alpha\gamma}$ set to 140 kJ/mol,[25] the pre-factor is fitted using the measured transformation kinetics at the later stage of austenite formation (austenite fraction above 0.20) where the ferrite-to-austenite transformation is dominant.

Consistency of the simulated transformation kinetics and microstructures with the experimental measurements is obtained as illustrated in Figures 6, 7, and 8. In particular, the simulated microstructures at the inter-

mediate stages of austenite formation are consistent with the metallographic observations in terms of the austenite morphology (Figure 7). A network of austenite grains is formed decorating the ferrite grain boundaries when the heating rate is 1 K/s (°C/s) in Case A (Figures 7(a) and (b)). In Case C where the heating rate is 100 K/s (°C/s), on the other hand, banded austenite morphology is obtained (Figures 7(c) and (d)). The agreement of austenite morphology with experiments in Case A, *i.e.*, complete occupation of ferrite grain boundaries by austenite grains, validates the postulated nucleation model that is tuned using the experimental data of Case

C. Site saturation of austenite nucleation at ferrite grain boundaries in Case A and rare nucleation in Case C indicates a comparatively weak temperature dependence of austenite nucleation which is in contrast to the austenite-to-ferrite transformation during continuous cooling where fast cooling usually stimulates more nucleation than slow cooling.

The adjustable parameters to reach this agreement are listed in Table II. The fitted activation energy of the pearlite/austenite interface mobility is comparatively high, reflecting a significant increase of the pearlite-to-
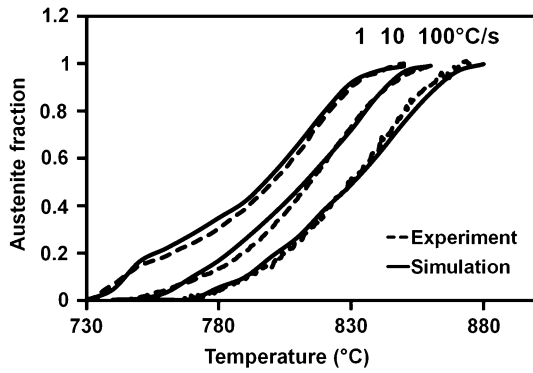

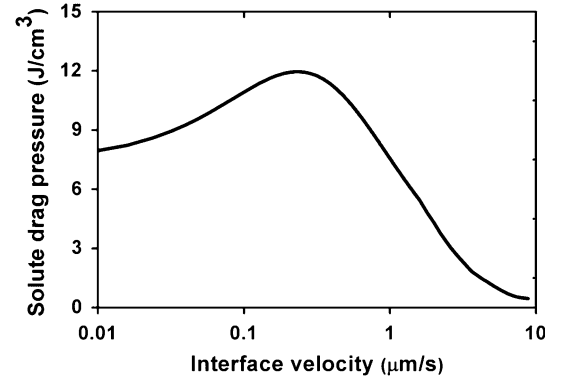Fig. 6—Comparison of austenite formation kinetics in experiments and simulations.

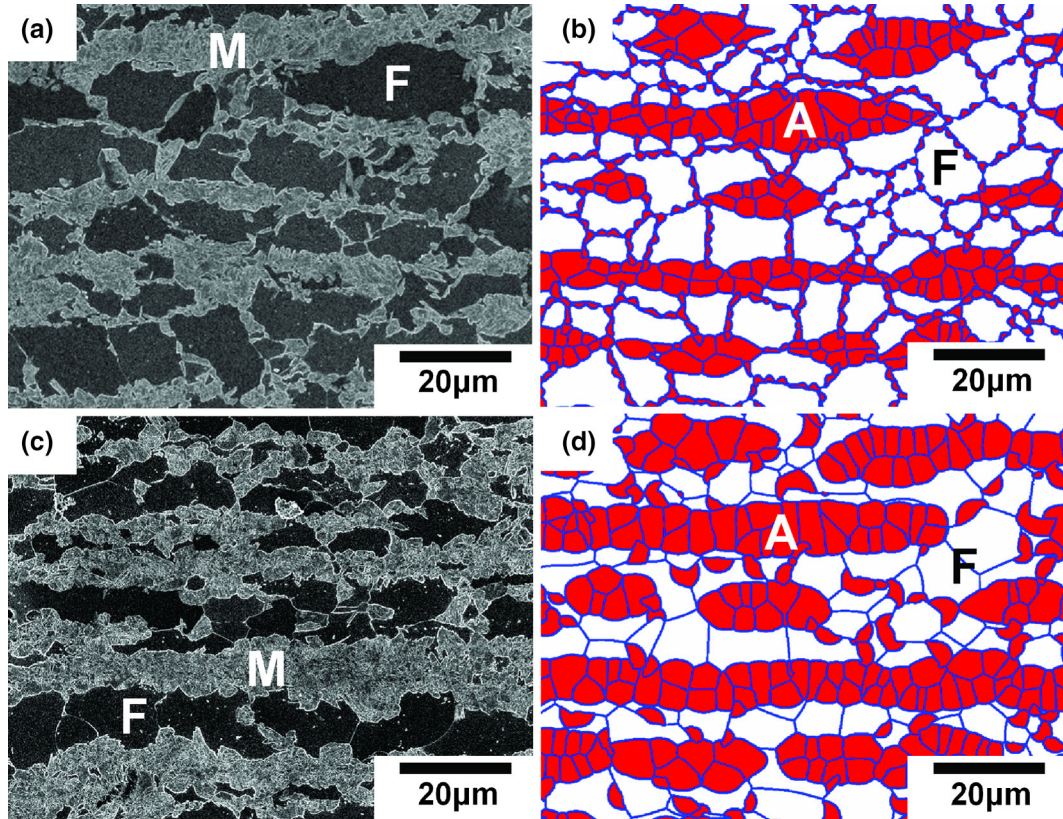Fig. 8—Solute drag pressure of Mn on the ferrite/austenite interface at 1043 K (770 °C).

Fig. 7—Comparison of experimental and simulated microstructures (A: austenite, F: ferrite, and M: martensite) for heating scenarios A at 1063 K (790 °C) (*a, b*) and C at 1098 K (825 °C) (*c, d*).

austenite transformation rate with temperature which is consistent with the findings of Speich *et al.*[32]

Figure 8 demonstrates the variation of solute drag pressure with interface velocity at 1043 K (770 °C). The solute drag is significant at lower velocities (<1 μm/s) and becomes gradually insignificant with increasing velocities (>1 μm/s). The simulations reveal that solute drag has a great effect on the transformation kinetics for slow and medium heating rates (1 to 10 K/s (°C/s)) where the interface velocity is in a range of 0.03 to 0.5 μm/s but not for the fast heating rate (100 K/s (°C/s)) where the driving pressure is sufficiently high such that the interface velocity is in a range of 2 to 10 μm/s with negligible solute drag. For example, in the case of 1 K/s (°C/s), the chemical driving pressure is about 9 J/cm^3 at 1043 K (770 °C) and the solute drag force is about 8.5 J/cm^3 with an interface velocity of 0.03 μm/s such that the effective driving pressure is 0.5 J/cm^3, only 5 pct of the chemical driving pressure. On the other hand, in the case of 100 K/s (°C/s), the chemical driving pressure is about 20 J/cm^3 at 1043 K (770 °C) and the solute drag pressure is about 2 J/cm^3 with an interface velocity of 4 μm/s, such that the effective driving pressure is 90 pct of the chemical driving pressure, *i.e.*, insignificant solute drag.

The good description of transformation kinetics also indicates that the values of binding energy and trans-interface diffusivity of Mn used in the model are reasonable. It is important to note that neglecting solute drag would have led to an interface mobility with an unrealistic dependence on heating rate to replicate the experimental austenite formation kinetics. Similar observations have been made elsewhere for continuous cooling austenite-to-ferrite transformations in low-carbon steels with apparent interface mobilities that depend on cooling rate unless solute drag is considered.[22]

Further, the simulations demonstrate that austenite grain growth is significant at lower heating rates. For example, at 1 K/s (°C/s), the total number of austenite nuclei introduced into the domain is about 900, but only 150 grains remain when full austenitization is attained. In particular, austenite grains nucleated at pearlite regions coarsen predominantly to sweep those formed at ferrite grain boundaries. A comparison of the measured and simulated final austenitic structures is shown in Figure 9.

C. *Austenite Formation During Rapid Continuous Heating*

During rapid continuous heating scenarios, austenite formation may not start from a well-annealed microstructure, *i.e.*, ferrite recrystallization may be incomplete and also the pearlite morphology may be different.[15] After heating at 1 K/s (°C/s) until 1003 K (730 °C), pearlite is partially spheroidized while the lamellar structure is retained during rapid heating, *e.g.*, a heating rate of 100 K/s (°C/s).[15] It was further observed that the pearlite dissolution temperature decreases from 1053 K (780 °C) in heating path B to 1033 K (760 °C)
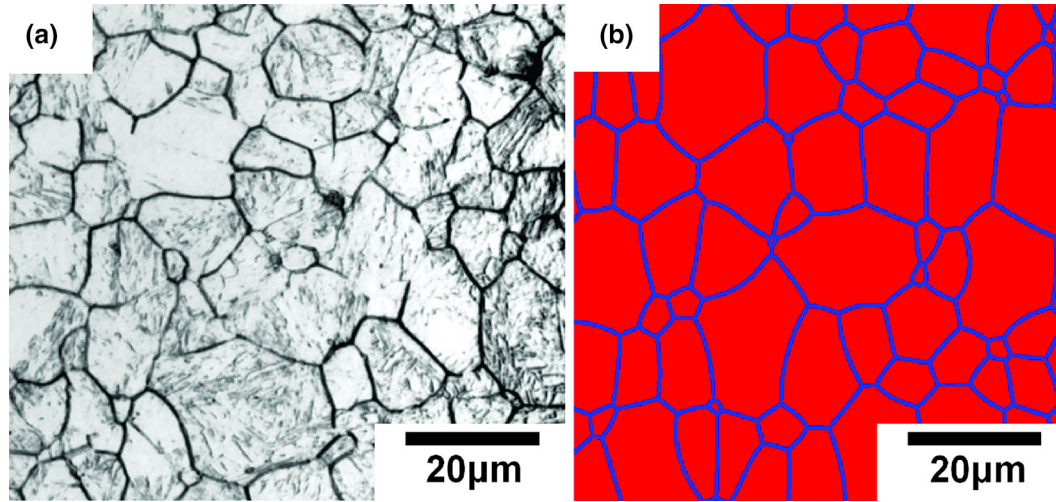

Fig. 9—Comparison of (*a*) experimental and (*b*) simulated final austenite microstructures at 1143 K (870 °C) for heating scenario A.

Table II. Values of Adjustable Parameters in the Model of Austenite Formation

Parameter	Symbol	Value
Austenite nuclei density in pearlite	N_P^i (μm^{-2})	2.4×10^{-2}
Nucleation parameter in the classic nucleation model	λ (1/s)	2.0×10^7
Pre-factor of pearlite/austenite interface mobility	$m_{P\gamma}^0$ (m^4/Js)	2.0×10^7
Activation energy of pearlite/austenite interface mobility	$Q_{P\gamma}$ (kJ/mol)	398
Pre-factor of ferrite/austenite interface mobility	$m_{\alpha\gamma}^0$ (m^4/Js)	5.0×10^{-6}
Pre-factor of austenite/austenite interface mobility	$m_{\gamma\gamma}^0$ (m^4/Js)	5.0×10^{-3}

in heating path D, and from 1073 K (800 °C) in heating path C to 1033 K (760 °C) in heating path E.[15] One cause of the faster transformation of pearlite to austenite during rapid continuous heating may thus be related to a lower degree of spheroidization and the higher level of interfacial energy remaining in the pearlite colonies. Further, slower transformation of pearlite to austenite at lower heating rates may also be related to an increased stability of cementite due to enhanced content of Mn and Cr that is partitioned to cementite during spheroidization.[33]

Regardless of the complicated physics behind the phenomenon mentioned above, the accelerated pearlite-to-austenite transformation can for simplicity be described by introducing an effective pearlite/austenite interface mobility that increases with heating rate by varying the pre-factor while keeping the activation energy the same as for the step-heating scenario. Increasing the pearlite/austenite interface mobility of the step-heating scenario (including the 1 K/s (°C/s) continuous heating case) by a factor 2 and 5 for heating rates of 10 K/s (°C/s) (Case D) and 100 K/s (°C/s) (Case E), respectively, permits to describe the experimentally observed acceleration of the pearlite-to-austenite transformation. Based on these values, a simple power function is proposed for the mobility pre-factor as a function of heating rate:

$$m^0_{P\gamma} = m^0_{P\gamma,1°C/s} \left(\frac{dT}{dt}\right)^{0.35} \qquad [15]$$

where $m^0_{P\gamma,1°C/s}$ is the value of the mobility pre-factor for a heating rate of 1 K/s (°C/s) that is relevant for the step-heating scenario (Table II). Combining this modification for the austenite-to-pearlite transformation with the phase-field model for the ferrite-to-austenite transformation developed for the step-heating scenario enables to predict satisfactorily the overall transformation kinetics without any further adjustments (Figure 10). It is found that ferrite recrystallization is completed at 1043 K (770 °C) in Case D, overlapping a little with austenite formation, while ferrite recrystallization proceeds concurrently with austenite formation until 1103 K (830 °C) in Case E. The contribution of stored energy in non-recrystallized ferrite to the transformation kinetics was found to be negligible in Case E. The main reason is that the chemical driving force for ferrite/austenite transformation in Case E is relatively high (15 to 30 MJ/m^3) in comparison with the average stored energy in the non-recrystallized ferrite grains (~2 MJ/m^3).

In the transformation of deformed austenite to ferrite, carbon diffusion in deformed austenite may be enhanced due to the presence of dislocations and other defects and, as a result, may contribute to the acceleration of transformation.[34] Whether or not enhanced carbon diffusion in ferrite could accelerate austenite formation has been tested with the model by increasing the carbon diffusivity in ferrite by a factor 100. No acceleration of transformation rate is found, which is reasonable because ferrite has a low carbon solubility, and carbon diffusion in ferrite is already much faster (~100 times)
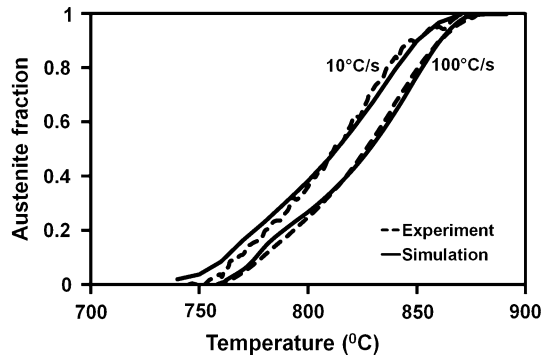

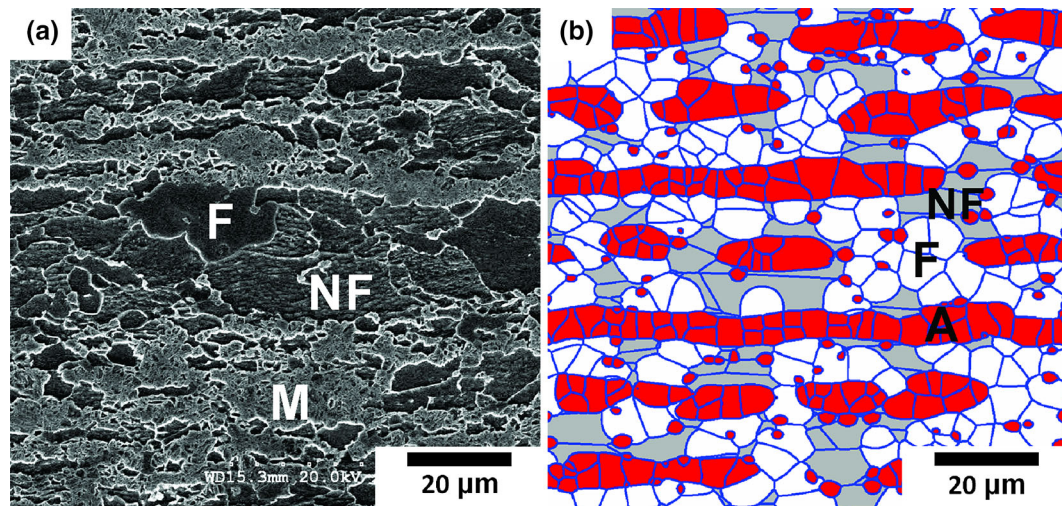Fig. 10—Comparison of measured and simulated transformation kinetics for heating scenarios D and E.

Fig. 11—Comparison of (a) experimental and (b) simulated microstructures at 1073 K (800 °C) for heating scenario E (A: austenite, F: recrystallized ferrite, NF: non-recrystallized ferrite, and M: martensite).
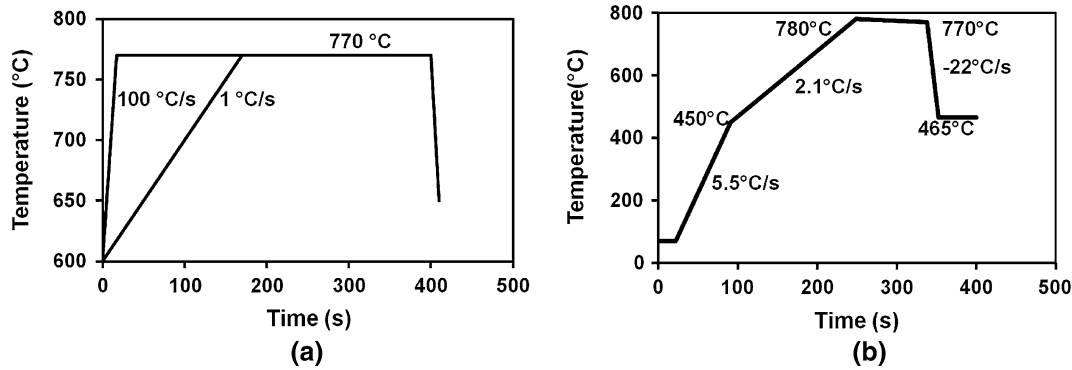
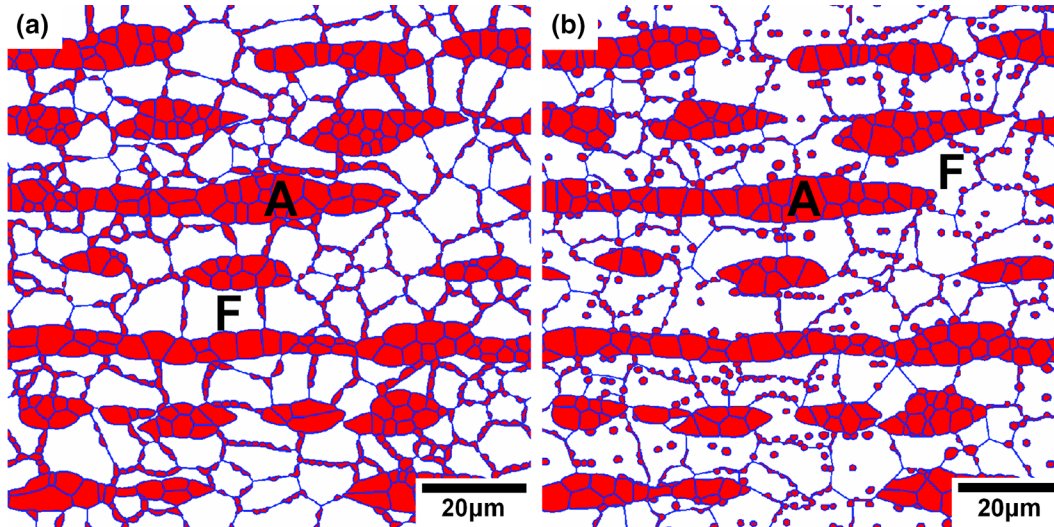Fig. 12—Thermal cycles of intercritical annealing used in the phase-field simulations.

Fig. 13—Simulated microstructures after intercritical annealing at 1043 K (770 °C) for 300 s with different heating rates: (*a*) 1 K/s (°C/s) and (*b*) 100 K/s (°C/s) (A: austenite, F: ferrite).

than that in austenite. Therefore, similar to the austenite-to-ferrite transformation, carbon diffusion in ferrite is not the rate-limiting factor for the ferrite-to-austenite transformation.

A comparison of simulated and experimental micrographs for continuous heating of 100 K/s (°C/s) is shown in Figure 11, exhibiting microstructures at an intermediate stage [1068 K (795 °C)]. It is evident that ferrite recrystallization and austenite formation occur simultaneously. In spite of some austenite grains nucleating at ferrite grain boundaries, austenite mainly forms in prior pearlite area, inheriting the banded morphology of pearlite. From the simulated microstructure, it can be observed that austenite grains can act as barriers to inhibit migration of recrystallization fronts. Some austenite grains even can pin the recrystallization fronts which also can be seen in the experimental micrograph. Another interesting observation is that some austenite grains are located inside recrystallized ferrite grains due to migration of recrystallization fronts, creating an illusion of intragranular nucleation of austenite in ferrite grains which had been previously attributed to the possible presence of carbides.[35]
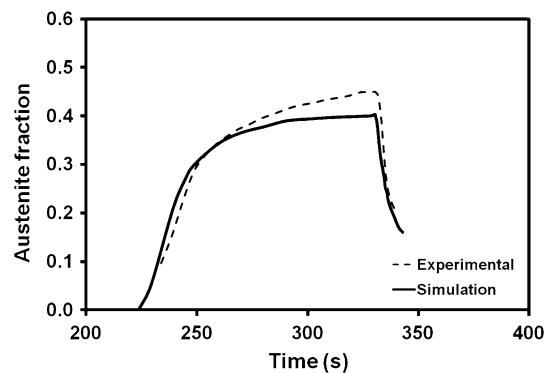

Fig. 14—Comparison of measured and simulated transformation kinetics in the industrial annealing cycle.

D. Intercritical Annealing

Three heating scenarios are used to study the intercritical annealing process (Figure 12). First, two simulations of isothermal intercritical annealing at 1043 K (770 °C) with two different initial heating rates, *i.e.*, 1 and 100 K/s (°C/s), are carried out to examine the effects

of heating rate on the austenite morphology (Figure 12(a)). Second, a selected industrial intercritical annealing cycle is simulated (Figure 12(b)) starting from 873 K (600 °C) where ferrite recrystallization initiates, and stopping at 738 K (465 °C) before the isothermal galvanizing process where bainite formation occurs that is not considered in the present model.

Figure 13 demonstrates the effect of the heating rate on the microstructure during intercritical annealing at 1043 K (770 °C). Similar to the continuous heating scenario, ferrite recrystallization overlaps with austenite formation for the heating rate of 100 K/s (°C/s).

However, ferrite recrystallization completes within the first 10 s holding at 1043 K (770 °C). On the other hand, for the heating rate of 1 K/s (°C/s), ferrite recrystallization completes before austenite formation. The total number of austenite nuclei in the simulation domain is about 900 for both cases. However, the locations of austenite nuclei are different. For the heating rate of 1 K/s (°C/s), austenite nuclei occupy prior pearlite regions and the recrystallized ferrite grain boundaries completely, forming a network morphology which is similar to the step-heating scenario. For the heating rate of 100 K/s (°C/s), austenite nucleation first occurs at the
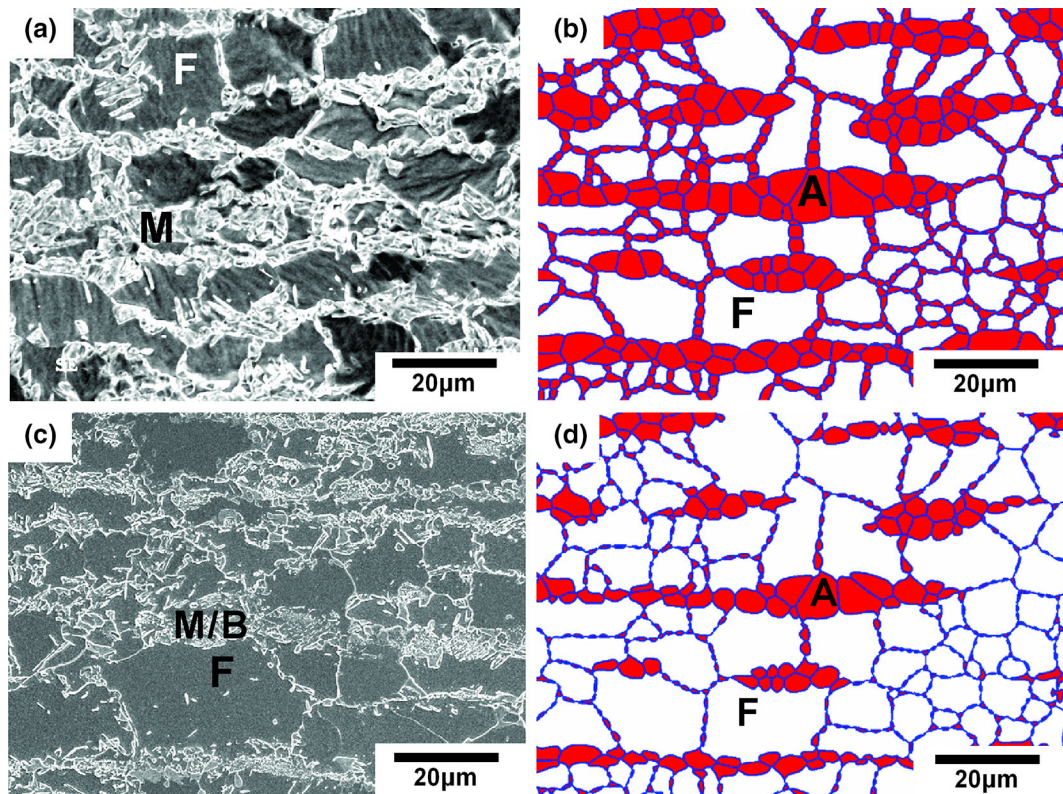

Fig. 15—Comparison of experimental micrographs and simulated microstructures at various stages of the industrial annealing cycle (A: austenite, B: bainite, F: ferrite, and M: martensite): (a–b): 1043 K (770 °C); (c–d): 738 K (465 °C).
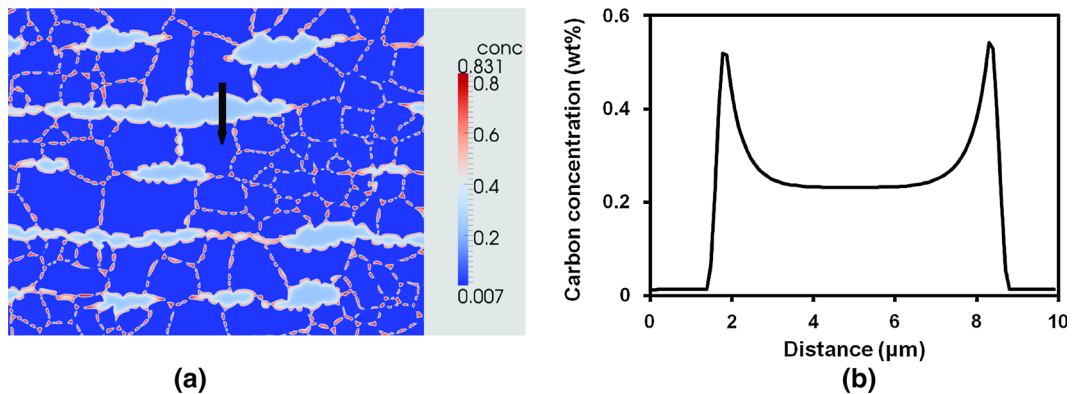

Fig. 16—Carbon concentration field (a) and a line plot (b) along the black arrow when reaching 738 K (465 °C) in the industrial intercritical annealing cycle.

pearlite/ferrite interfaces and deformed ferrite grain boundaries, leading to both intergranular and intragranular distribution of austenite grains. Intragranular austenite grains are arranged in arrays parallel to the rolling direction. These austenite grains are formed originally at the deformed ferrite grain boundaries. Later, as the recrystallization fronts sweep the old grain boundaries, these austenite grains are left inside the recrystallized ferrite grains.

For the simulation of the industrial annealing cycle, both the predicted transformation kinetics and the microstructures are in reasonable agreement with the experimental results (Figures 14 and 15). Similar to slow heating scenarios, many austenite grains decorate recrystallized ferrite grain boundaries. Before fast cooling, the austenite fraction has reached 0.40 at 1043 K (770 °C), consistent with the experimental measurement (0.45 ± 0.05). During fast cooling, epitaxial ferrite grows into austenite, leading to an austenite fraction of 0.20 at 738 K (465 °C). But it should be noted that in the experimental micrograph (Figure 15(c)), some austenite has already transformed into bainite during cooling which is not considered in the phase-field model. It is also found that the carbon concentration is rather high in a narrow region of austenite in front of the α/γ interface compared with the interior, due to insufficient diffusion in austenite during fast cooling (Figure 16). This could provide an explanation of the experimental observation that bainite is often surrounded by a rim of martensite in the prior austenite region.

IV. CONCLUSIONS

In this work, a 2D phase-field model has been developed to simulate austenite formation and its interaction with ferrite recrystallization during heating of a cold-rolled ferrite-pearlite steel. A solute drag model is coupled to the phase-field model to enable the description of the austenite formation kinetics as a function of heating rate. The interaction of ferrite recrystallization and austenite formation has also been studied, revealing that spheroidization of deformed pearlite prior to austenite formation decelerates overall austenite formation. The simulations have duplicated the microstructural change of the austenite phase from network morphology to banded morphology with increasing heating rates. Furthermore, the well-tuned phase-field model has been successfully applied to industrial intercritical annealing cycles, predicting the dual-phase microstructures and transformation kinetics.

Overall, the present study indicates that phase-field models are a promising computational approach to simulate microstructure evolution during intercritical annealing of advanced high-strength steels.

REFERENCES

1. C. Bos, M.G. Mecozzi, D.N. Hanlon, M.P. Aarnts, and J. Sietsma: *Metall. Mater. Trans. A*, 2011, vol. 42A, pp. 3602–10.
2. D. Liu, F. Fazeli, and M. Militzer: *ISIJ Int.*, 2007, vol. 47, pp. 1789–98.
3. D. Bombac, M.J. Peet, S. Zenitani, S. Kimura, T. Kurimura, and H.K.D.H. Bhadeshia: *Model. Simul. Mater. Sci. Eng.*, 2014, vol. 22, p. 045005(14).
4. C. Bos, M.G. Mecozzi, and J. Sietsma: *Comput. Mater. Sci.*, 2010, vol. 48, pp. 692–699.
5. J. Rudnizki, B. Böttger, U. Prahl, and W. Bleck: *Metall. Mater. Trans. A*, 2011, vol. 42A, pp. 2516–25.
6. M. Kulakov, W.J. Poole, and M. Militzer: *Metall. Mater. Trans. A*, 2013, vol. 44A, pp. 3564–76.
7. H. Azizi-Alizamini, M. Militzer, and W.J. Poole: *Metall. Mater. Trans. A*, 2010, vol. 42A, pp. 1544–57.
8. J. Huang, W. Poole, and M. Militzer: *Metall. Mater. Trans. A*, 2004, vol. 35A, pp. 3363–75.
9. C. Zheng and D. Raabe: *Acta Mater.*, 2013, vol. 61, pp. 5504–5517.
10. M. Kulakov: Ph.D. Thesis, University of British Columbia, Vancouver, Canada, 2013.
11. I. Steinbach and F. Pezzolla: *Phys. Nonlinear Phenom..*, 1999, vol. 134 (4), pp. 385–93.
12. J. Eiken, B. Böttger, and I. Steinbach: *Phys. Rev. E*, 2006, vol. 73 (6), p. 066122(9).
13. B. Zhu and M. Militzer: *Model. Simul. Mater. Sci. Eng.*, 2012, vol. 20 (8), p. 085011(17).
14. A. Godfrey, N. Hansen, and D. Juul Jensen: *Metall. Mater. Trans. A*, 2007, vol. 38A, pp. 2329–39 .
15. M. Kulakov: The University of British Columbia, Vancouver, Canada, Private Communication, 2014.
16. D. Raabe and L. Hantcherli: *Comput. Mater. Sci.*, 2005, vol. 34 (4), pp. 299–313.
17. D. Raabe and R.C. Becker: *Model. Simul. Mater. Sci. Eng.*, 2000, vol. 8 (4), p. 445.
18. D. Raabe: *Annu. Rev. Mater. Res.*, 2002, vol. 32 (1), pp. 53–76.
19. M. Sánchez-Araiza, S. Godet, P.J. Jacques, and J.J. Jonas: *Acta Mater.*, 2006, vol. 54 (11), pp. 3085–93.
20. V. Savran, S. Offerman, and J. Sietsma: *Metall. Mater. Trans. A*, 2010, vol. 41A, pp. 583–91.
21. H.I. Aaronson, W.F. Lange, III, and G.R. Purdy: *Scripta Mater*, 2004, vol. 51 (9), pp. 931–35.
22. I. Lischewski and G. Gottstein: *Acta Mater.*, 2011, vol. 59 (4), pp. 1530–41.
23. J Warren, T Pusztai, L Környei, and L Gránásy: *Phys. Rev. B*, 2009, vol. 79 (1), p. 014204.
24. L Gránásy, T Pusztai, D Saylor, and J Warren: *Phys. Rev. Lett.*, 2007, vol. 98 (3), p. 035703.
25. M. Militzer: *Curr. Opin. Solid State Mater. Sci.*, 2011, vol. 15 (3), pp. 106–15.
26. M. Hillert and B. Sundman: *Acta Metall.*, 1976, vol. 24 (8), pp. 731–43.
27. J.W. Cahn: *Acta Metall.*, 1962, vol. 10 (9), pp. 789–98.
28. G.R. Purdy and Y.J.M. Brechet: *Acta Metall. Mater.*, 1995, vol. 43 (10), pp. 3763–74.
29. T. Jia and M. Militzer: *ISIJ Int.*, 2012, vol. 52 (4), pp. 644–49.
30. H. Chen, K. Zhu, L. Zhao, and S. van der Zwaag: *Acta Mater.*, 2013, vol. 61 (14), pp. 5458–68.
31. R.G. Thiessen, J. Sietsma, T.A. Palmer, J.W. Elmer, and I.M. Richardson: *Acta Mater.*, 2007, vol. 55 (2), pp. 601–14.
32. G. Speich, V. Demarest, and R. Miller: *Metall. Trans. A*, 1981, vol. 12A, pp. 1419–28.
33. W. Song, P.-P. Choi, G. Inden, U. Prahl, D. Raabe, and W. Bleck: *Metall. Mater. Trans. A*, 2014, vol. 45A, pp. 595–606.
34. Y.J. Lan, N.M. Xiao, D.Z. Li, and Y.Y. Li: *Acta Mater.*, 2005, vol. 53 (4), pp. 991–1003.
35. D. Yang, E. Brown, D. Matlock, and G. Krauss: *Metall. Trans. A*, 1985, vol. 16, pp. 1385–92.